

# Iridium single atoms incorporated in $\text{Co}_3\text{O}_4$ efficiently catalyze the oxygen evolution in acidic conditions

Received: 13 July 2022

Accepted: 2 December 2022

Published online: 14 December 2022



Yiming Zhu<sup>1,6</sup>, Jiaao Wang<sup>2,6</sup>, Toshinari Koketsu<sup>1,3</sup>, Matthias Kroschel<sup>3</sup>, Jin-Ming Chen<sup>4</sup>, Su-Yang Hsu<sup>4</sup>, Graeme Henkelman<sup>2</sup>, Zhiwei Hu<sup>5</sup>✉, Peter Strasser<sup>3</sup>✉ & Jiwei Ma<sup>1</sup>✉

Designing active and stable electrocatalysts with economic efficiency for acidic oxygen evolution reaction is essential for developing proton exchange membrane water electrolyzers. Herein, we report on a cobalt oxide incorporated with iridium single atoms ( $\text{Ir-Co}_3\text{O}_4$ ), prepared by a mechanochemical approach. Operando X-ray absorption spectroscopy reveals that Ir atoms are partially oxidized to active  $\text{Ir}^{>4+}$  during the reaction, meanwhile Ir and Co atoms with their bridged electrophilic O ligands acting as active sites, are jointly responsible for the enhanced performance. Theoretical calculations further disclose the isolated Ir atoms can effectively boost the electronic conductivity and optimize the energy barrier. As a result,  $\text{Ir-Co}_3\text{O}_4$  exhibits significantly higher mass activity and turnover frequency than those of benchmark  $\text{IrO}_2$  in acidic conditions. Moreover, the catalyst preparation can be easily scaled up to gram-level per batch. The present approach highlights the concept of constructing single noble metal atoms incorporated cost-effective metal oxides catalysts for practical applications.

Centuries of industrialization and human activities have consumed enormous amounts of fossil fuels, which has inevitably led to the current energy crisis and global warming<sup>1</sup>. Hydrogen ( $\text{H}_2$ ) is considered a promising alternative energy carrier of the future owing to its high energy density and potential for carbon-free emission<sup>2</sup>. Among many  $\text{H}_2$  production methods, water electrolysis has received much attention as a feasible technology for practical applications. Nevertheless, due to the sluggish kinetics of the complex four-electron transfer process, the oxygen evolution reaction (OER) at the anode side of the water electrolyzer demonstrates high overpotentials, which severely limit the overall operation efficiency and impede the large commercialization of water electrolyzers<sup>3–6</sup>. Therefore, tremendous effort has

been devoted to the rational design of robust electrocatalysts which improve the OER activity and energy conversion efficiency.

Over the past few decades, the noble metal oxides based on iridium (Ir) and ruthenium (Ru) are considered the state-of-the-art OER electrocatalysts. However, their widespread applications are limited by the cost and scarcity of Ir and Ru<sup>7–10</sup>. As a result, the first row 3d transition metal oxides and their derivatives, with merits of high abundance and low cost have received much attention as alternative OER candidates<sup>11–15</sup>. Among all 3d transition metal oxides, cobalt-based oxides such as spinel  $\text{Co}_3\text{O}_4$  have been widely used to activate OER activity, as demonstrated by both experimental data and theoretical calculations<sup>16–19</sup>. Nevertheless,  $\text{Co}_3\text{O}_4$  still suffers from an overpotential

<sup>1</sup>Shanghai Key Laboratory for R&D and Application of Metallic Functional Materials, Institute of New Energy for Vehicles, School of Materials Science and Engineering, Tongji University, Shanghai 201804, China. <sup>2</sup>Department of Chemistry and the Oden Institute for Computational Engineering and Sciences, The University of Texas at Austin, Austin, TX 78712-0165, USA. <sup>3</sup>Department of Chemistry, Technical University Berlin, 10623 Berlin, Germany. <sup>4</sup>National Synchrotron Radiation Research Center, Hsinchu 30076, Taiwan. <sup>5</sup>Max Planck Institute for Chemical Physics of Solids, Nöthnitzer Strasse 40, 01187 Dresden, Germany.

<sup>6</sup>These authors contributed equally: Yiming Zhu, Jiaao Wang. ✉e-mail: [zhiwei.hu@cpfs.mpg.de](mailto:zhiwei.hu@cpfs.mpg.de); [pstrasser@tu-berlin.de](mailto:pstrasser@tu-berlin.de); [jiwei.ma@tongji.edu.cn](mailto:jiwei.ma@tongji.edu.cn)

of more than 400 mV for the OER at a current density of  $10 \text{ mA cm}^{-2}$ , which is far from meeting the requirements for practical applications. Moreover,  $\text{Co}_3\text{O}_4$  is unstable under the harsh OER conditions at the high oxidizing potential in corrosive media such as an acidic electrolyte<sup>20–22</sup>. It is well known that the 4d/5d noble elements possess a large *d*-electronic wave-function spatial extent, generating versatile electronic structures via the interaction between 3d and 4d/5d orbitals, which is beneficial for enhancing OER activity. One available method that has been frequently used is incorporating bulk amounts of noble metals with Co or its derivatives to obtain hybrid 3d/4d or 3d/5d nanomaterials as OER electrocatalysts<sup>23–25</sup>. In this regard, Li et al. reported that the  $\text{Sr}_2\text{CoIrO}_{6.8}$ , which benefits from a synergy between Co and Ir active sites, exhibits a low overpotential toward OER<sup>26</sup>. Pi and co-workers also demonstrated that IrCo bimetallic nanoclusters can be employed as efficient OER electrocatalysts<sup>27</sup>. In addition, Shah et al. developed a catalyst with single Co atoms doped on  $\text{RuO}_2$  sphere, yielding remarkable catalytic performances for water splitting<sup>28</sup>. Notwithstanding these efforts to modify Co-based nanomaterials as alternative OER catalysts, it remains difficult to tip the balance between low cost and high performance. Recently, the strategy of constructing highly dispersed single-sites catalysts has attracted significant attentions for a range of electrocatalytic reactions<sup>29</sup>. Downsizing the materials into isolated atoms is beneficial for reducing the amount of bulk metal, which can greatly maximize the atom-utilization efficiency, leading to remarkable catalytic mass activity<sup>30–32</sup>. Additionally, the unique electronic structure of uniformly dispersed active sites usually results in a strong interaction with the host material, effectively adjusting the electrochemical microenvironment over catalysts and potentially boosting the electrocatalytic activity<sup>33–35</sup>. Motivated by the abovementioned guidelines, the integration of spinel Co-based oxide with noble metal single atoms as the prospective OER electrocatalyst, possesses advantages of minimized noble metal usage and optimized catalytic performances. Nevertheless, the large lattice discrepancy between the diverse atoms and strong binding energy between the same atoms, are great challenges to disperse homogeneous noble metal single sites in the transition metal oxide host<sup>36</sup>. And the production of traditional methods to prepare the single-atom materials such as impregnation are usually limited to milligram level, it is extremely urgent to explore a mass-production method to meet the requirements for practical applications.

In this work, we deploy a facile and economical strategy to prepare atomically dispersed Ir atoms doped in spinel  $\text{Co}_3\text{O}_4$  ( $\text{Ir-Co}_3\text{O}_4$ ) via a mechanochemical method. By introducing a trace amount of Ir (–1.05 at%),  $\text{Ir-Co}_3\text{O}_4$  displays a remarkable OER overpotential of 236 mV in an acid medium at the current density of  $10 \text{ mA cm}^{-2}$ , which is significantly lower than that of as-prepared  $\text{Co}_3\text{O}_4$  (412 mV). Significantly, both the normalized mass activity and TOF of  $\text{Ir-Co}_3\text{O}_4$  can reach almost two order magnitudes higher than those of commercial  $\text{IrO}_2$  at an overpotential of 300 mV, respectively. Meanwhile, the stability can also be extended much longer after incorporating Ir single atoms within the lattice of  $\text{Co}_3\text{O}_4$ . Using operando X-ray absorption near edge structure (XANES) at the Ir-*L*<sub>3</sub> and Co-*K* edges, it is observed that the Ir species are partially oxidized to OER-active  $\text{Ir}^{3+4+}$ , and the elevated valence states with increased voltage also indicate that both high-valence Ir and Co atoms with their bridged electrophilic O ligands serve as active sites, which are jointly responsible for charge transfer in electrochemical reactions. In addition, density functional theory (DFT) calculations confirm the improved electronic conductivity and facile energy barrier contributed by the incorporated Ir single atoms, resulting in a high OER catalytic activity. Moreover, the preparation of  $\text{Ir-Co}_3\text{O}_4$  can be easily scaled up to achieve gram-level per batch with negligible activity loss, demonstrating this strategy as an economical approach to prepare advanced electrocatalysts in a larger scale for practical applications.

## Results

### Structural characterizations of $\text{Ir-Co}_3\text{O}_4$

$\text{Ir-Co}_3\text{O}_4$  was synthesized based on the mechanochemical method, in which a solid solution of NaCl and metal precursors were formed by ball milling and then calcination (see Methods for details). The morphology of  $\text{Ir-Co}_3\text{O}_4$  was initially characterized by scanning electron microscopy (SEM). As shown in Fig. 1a,  $\text{Ir-Co}_3\text{O}_4$  reveals nanosized and flake morphology. Typical transmission electron microscopy (TEM) images show that  $\text{Ir-Co}_3\text{O}_4$  is structured as flexible ultrathin nanosheets with thickness of about 3 nm as indicated by atomic force microscopy (AFM) images. The ultrathin 2D structure of  $\text{Ir-Co}_3\text{O}_4$  can potentially maximize the exposed active sites on the surface and increase the contact area with the electrolyte, leading to the enhanced catalytic performance (Fig. 1b, c & Supplementary Fig. 1)<sup>37</sup>. Detailed structural analysis by high-resolution TEM (HR-TEM) confirms that  $\text{Ir-Co}_3\text{O}_4$  has lattice spacings of 2.48 Å and 3.02 Å, which can be ascribed to the  $\text{Co}_3\text{O}_4$  (311) and (220) facets, respectively. Furthermore, due to the introduction of NaCl as the hard template in preparation, pores are generated and can be observed in the lattice structure of  $\text{Ir-Co}_3\text{O}_4$ . In general, those mesopores often result in more exposed active atoms on the edge, which are favorable for catalytic activity (Fig. 1d & Supplementary Fig. 2)<sup>38</sup>. Meanwhile, pure  $\text{Co}_3\text{O}_4$  synthesized by the same method exhibits no evident differences in morphology as compared with  $\text{Ir-Co}_3\text{O}_4$  (Supplementary Fig. 3). The crystal structures of  $\text{Ir-Co}_3\text{O}_4$  and as-synthesized  $\text{Co}_3\text{O}_4$  were characterized by X-ray diffraction (XRD) analysis, revealing similar patterns of face-centered cubic symmetry (space group:  $Fd\bar{3}m$ ) of the spinel structure. Rietveld refinements were further performed on those XRD patterns: the refined lattice parameters are  $a = 8.0972(5) \text{ Å}$ ,  $b = 8.0972(5) \text{ Å}$ ,  $c = 8.0972(5) \text{ Å}$ , and  $V = 530.89(6) \text{ Å}^3$  for  $\text{Ir-Co}_3\text{O}_4$ , as compared to  $a = 8.0754(3) \text{ Å}$ ,  $b = 8.0754(3) \text{ Å}$ ,  $c = 8.0754(3) \text{ Å}$ , and  $V = 526.61(3) \text{ Å}^3$  for as-prepared  $\text{Co}_3\text{O}_4$  (Supplementary Figs. 4, 5 & Supplementary Table 1, 2). The expanded crystal cells of  $\text{Ir-Co}_3\text{O}_4$  may be attributed to Ir atoms with a larger radius incorporated into the lattice of  $\text{Co}_3\text{O}_4$ . Subsequent composition evaluation of  $\text{Ir-Co}_3\text{O}_4$  by inductively coupled plasma-optical emission spectrometry (ICP-OES) and SEM energy-dispersive spectroscopy (SEM-EDS) confirms that Ir has an atomic ratio of 1.05% (Supplementary Fig. 6). In addition, the possible Fe impurity in  $\text{Ir-Co}_3\text{O}_4$  derived from the stainless-steel ball milling device was also determined to be 0.0667 wt% by ICP-OES, which can be ignored compared to the contents of other elements.

To determine the distribution of Ir species at the atomic scale, aberration corrected high angle annular dark field-scanning transmission electron microscopy (AC HAADF-STEM) images were collected on  $\text{Ir-Co}_3\text{O}_4$ . The corresponding fast Fourier transform (FFT) image identifies the exposure of (311), (311) and (022) planes of  $\text{Co}_3\text{O}_4$  along the [233] zone axis. Interestingly, high-magnification images demonstrate the presence of monodispersed Ir single atoms (bright dots marked by red circles in Fig. 1e, f). On account of the higher Z number, the Ir atom brightness is more intense than neighboring Co atoms<sup>39</sup>. The dispersion of isolated Ir atoms was further verified by the profiles along the dashed rectangles in the AC HAADF-STEM image, in which the different atomic intensities can be clearly distinguished (Fig. 1g). Additionally, the 3D atom-overlapping Gaussian function fitting mapping of the selected area in Fig. 1e is employed to observe the atomic distribution. As shown in Fig. 1h, the highest peaks representing Ir atoms are evenly dispersed, providing further evidence of isolated atoms. Elemental mapping images also show a homogeneous dispersion of Ir, Co, and O atoms throughout the entire  $\text{Ir-Co}_3\text{O}_4$  sample (Fig. 1i & Supplementary Fig. 7).

### Electronic and atomic structure analysis of $\text{Ir-Co}_3\text{O}_4$

To understand the electronic structure of  $\text{Ir-Co}_3\text{O}_4$ , we carried out X-ray photoelectron spectroscopy (XPS). All XPS spectra were

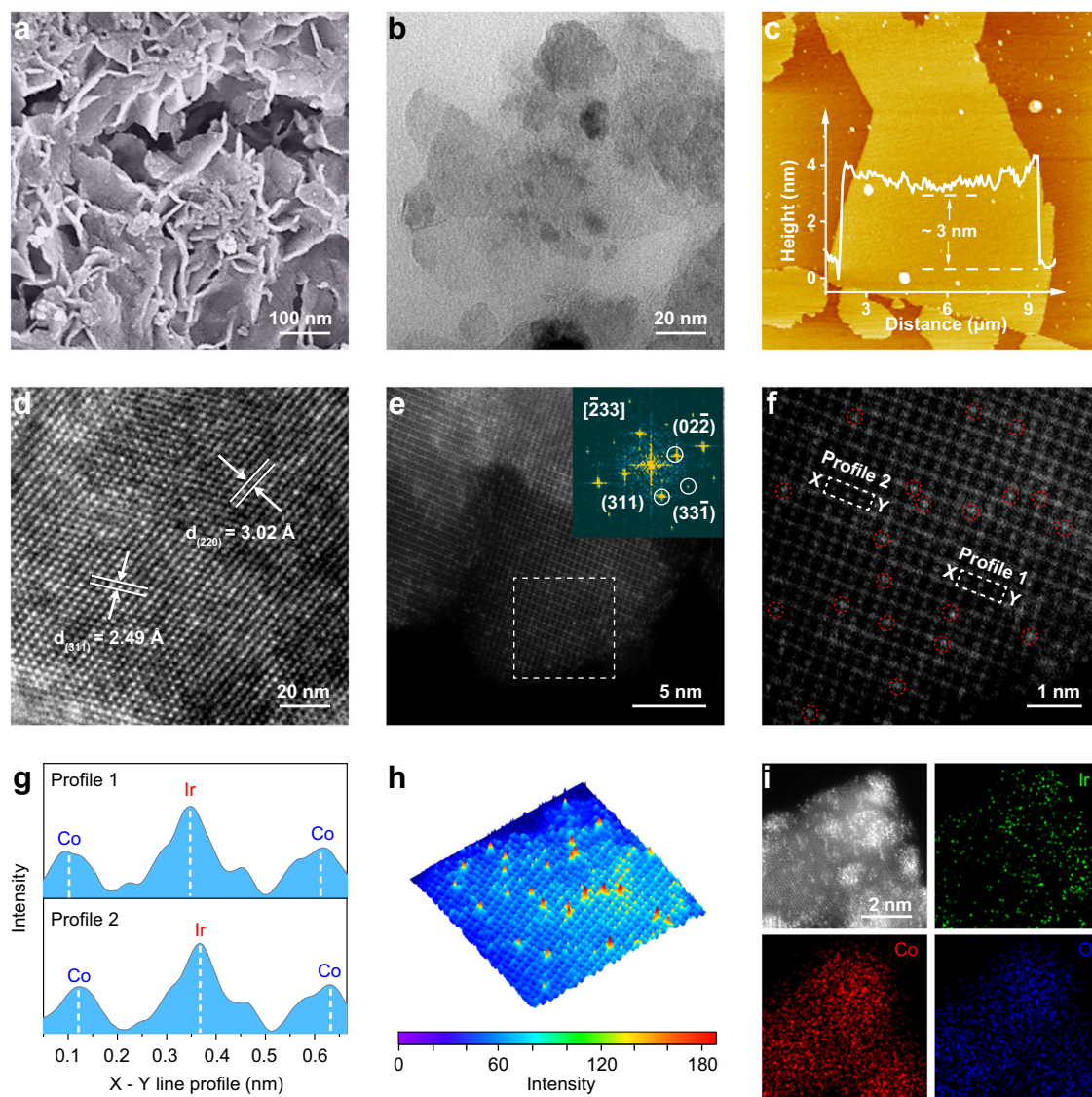


**Fig. 1 | Structural characterizations of Ir-Co<sub>3</sub>O<sub>4</sub>.** **a** SEM, **(b)** TEM, **(c)** AFM and **(d)** HR-TEM images of Ir-Co<sub>3</sub>O<sub>4</sub>. Inset in **(c)** is the height profile of Ir-Co<sub>3</sub>O<sub>4</sub> along the dashed line. **e** AC HAADF-STEM image and the corresponding FFT image (inset) of Ir-Co<sub>3</sub>O<sub>4</sub>. **f** The enlarged area in **(e)**, with the Ir single atoms marked in circles, and

**(g)** intensity profiles along the dashed rectangles. **h** 3D atom-overlapping Gaussian function fitting mapping of the selected area in **(e)**. **i** AC HAADF-STEM image and the corresponding elemental mappings of Ir-Co<sub>3</sub>O<sub>4</sub>.

calibrated with C 1s using a binding energy of 284.8 eV. The survey XPS spectra of Ir-Co<sub>3</sub>O<sub>4</sub> demonstrate the existence of Ir, Co and O elements on the surface (Supplementary Fig. 8). As shown in Fig. 2a, a typical IrO<sub>2</sub> XPS shows one sets of doublets at 62.5 and 65.4 eV, which can be attributed to Ir<sup>4+</sup>. For Ir-Co<sub>3</sub>O<sub>4</sub>, the Ir 4f spectrum can be deconvoluted into two sets of doublets centered at 61.8 / 63.7 eV and 62.4 / 65.3 eV, which can be attributed to Ir<sup>4+</sup> and Ir<sup>3+</sup>, respectively<sup>40–42</sup>. Accordingly, the Ir species on the surface of Ir-Co<sub>3</sub>O<sub>4</sub> is oxidized with chemical states between +3 and +4. The peak located at 60.6 eV is produced by Co 3p. The introduction of Ir affects the electronic structure of Co<sub>3</sub>O<sub>4</sub>; as revealed in Fig. 2b, the main peaks of Co 2p<sub>3/2</sub> of both Ir-Co<sub>3</sub>O<sub>4</sub> and as-synthesized Co<sub>3</sub>O<sub>4</sub> present signals that can be identified as Co<sup>2+</sup> and Co<sup>3+</sup>, respectively. Nevertheless, the Co<sup>2+</sup> over Co<sup>3+</sup> ratio is increased by 8.33 % after Ir species are introduced (the ratios of Co<sup>2+</sup>:Co<sup>3+</sup> in Co<sub>3</sub>O<sub>4</sub> and Ir-Co<sub>3</sub>O<sub>4</sub> are 0.48:1 and 0.52:1, respectively), suggesting a decreased valence state of Co on the surface of Ir-Co<sub>3</sub>O<sub>4</sub>. Moreover, since the incorporated Ir possesses stronger covalency, the O 1s XPS spectrum of Ir-Co<sub>3</sub>O<sub>4</sub> reveals a more positive binding energy and larger lattice oxygen M-O concentration than that of Co<sub>3</sub>O<sub>4</sub>, which is induced by the incorporation of Ir atoms (Fig. 2c)<sup>43</sup>.

X-ray absorption spectroscopy (XAS) was conducted with the aim of distinguishing the electronic structure and the local atomic environment of Ir-Co<sub>3</sub>O<sub>4</sub>. The energy position of the white line of X-ray absorption near edge structure (XANES) at the 5d transition metals is highly sensitive to their valence states<sup>44–48</sup>. And it is well known that an increase of the valence state of the 5d metal ion by one results in a shift of the L<sub>2,3</sub> XAS spectra by one or more eV toward higher energies<sup>44</sup>. Figure 2d shows the Ir L<sub>3</sub> XANES of Ir-Co<sub>3</sub>O<sub>4</sub> together with Ir foil and IrO<sub>2</sub> for comparison. One can observe that the white line of Ir-Co<sub>3</sub>O<sub>4</sub> shifts by 1.6 eV to a higher energy relative to Ir foil, but is located extremely close to that of IrO<sub>2</sub>, demonstrating that the Ir chemical state is close to +4, which is distinct from those in nanoparticles or supported single atoms. In addition, the white line intensity is in principle proportional to the d orbital density of states that are affected by the presence of multiple oxidation states and various electron configuration. The higher integrated white line intensity of Ir-Co<sub>3</sub>O<sub>4</sub> indicates that it has more empty d orbital states (d holes) than IrO<sub>2</sub>, which may lead to enhanced electrocatalytic performances. Importantly, the information derived from Ir L<sub>3</sub>-edge extended X-ray absorption fine structure (EXAFS) of Ir-Co<sub>3</sub>O<sub>4</sub> shows two distinct peaks



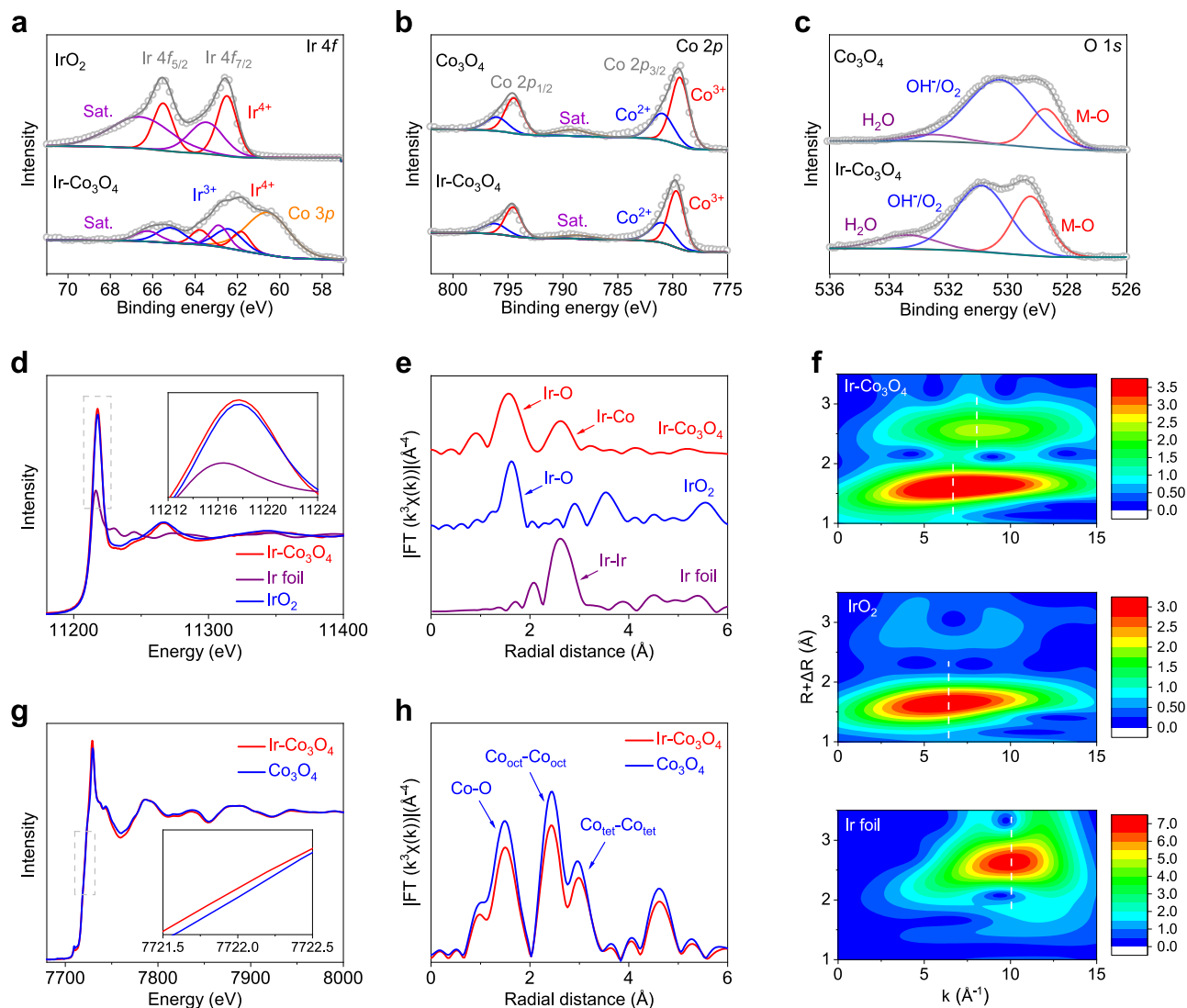


**Fig. 2 | Electronic and atomic structure analysis of Ir-Co<sub>3</sub>O<sub>4</sub>.** **a** Ir 4f XPS spectra of Ir-Co<sub>3</sub>O<sub>4</sub> and IrO<sub>2</sub>. **b** Co 2p XPS spectra and **(c)** O 1s XPS spectra of Ir-Co<sub>3</sub>O<sub>4</sub> and Co<sub>3</sub>O<sub>4</sub>. **d** XANES spectra of Ir-L<sub>3</sub> edge on Ir-Co<sub>3</sub>O<sub>4</sub>, Ir foil and IrO<sub>2</sub>. **e** The normalized Ir-L<sub>3</sub> edge XANES spectra of Ir-Co<sub>3</sub>O<sub>4</sub>, Ir foil and IrO<sub>2</sub>. **f** Ir-L<sub>3</sub> edge EXAFS spectra and

**(f)** corresponding wavelet-transformed  $k^3$ -weighted EXAFS spectra of Ir-Co<sub>3</sub>O<sub>4</sub>, Ir foil and IrO<sub>2</sub>. **g** The normalized Co-K edge XANES spectra and **(h)** Co-K edge XANES spectra of Ir-Co<sub>3</sub>O<sub>4</sub> and Co<sub>3</sub>O<sub>4</sub>.

in R space, in which the first peak can be clearly attributed to Ir-O bonds (Fig. 2e). The second bond cannot be distinguished directly due to the similar lengths of Ir-Ir bond (2.707 Å) and Ir-Co bond (2.91 Å) (discussed below). It was further recognized by the wavelet transform (WT)-EXAFS analysis, which exhibits two characteristic regions: a first shell domain for Ir-O scattering with a local maximum at  $R = 1.58$  Å and  $k = 6.62$  Å<sup>-1</sup> and a second shell domain at  $R = 2.61$  Å and  $k = 8.02$  Å<sup>-1</sup>. Although the second shell domain in Ir-Co<sub>3</sub>O<sub>4</sub> has a similar R value on that of Ir-Ir scattering in Ir foil ( $R = 2.65$  Å and  $k = 10.04$  Å<sup>-1</sup>), their k values are quite different, implying the existence of Ir-Co rather than Ir-Ir in the second shell scattering (Fig. 2f). Furthermore, a model-based EXAFS fit of Ir-Co<sub>3</sub>O<sub>4</sub>, IrO<sub>2</sub> and Ir foil were performed and the results indicate that no Ir-Ir scattering can be discovered and that the second scattering can be attributed to Ir-Co with a distinct bond distance, which represents Ir-O-Co in the crystal structure (Supplementary Fig. 9 & Supplementary Table 3). Therefore, based upon of advanced electronic microscopy and spectroscopic techniques, we conclude that the Ir species exist as single atoms and are homogeneously dispersed in the Co<sub>3</sub>O<sub>4</sub> host.

Unlike the XANES spectra at the 5d-L<sub>3</sub> edge, where the strong white line represents an unoccupied 5d state, the dominate peak at the 3d-K edge represents an unoccupied 4p state, whose energy position and shape are determined primarily by the crystal structure. In such a case, the valence state of 3d elements can be confirmed by the energy position of the leading edge (at a normalized absorption position of 0.8)<sup>48–50</sup>. The sensitivity of the absorption edge to the valence state of 3d elements originates from a relatively large  $U_{\text{cd}}$  (1s core hole and 3d Coulomb interaction) as compared with  $U_{\text{dp}}$  (3d and 4p Coulomb interactions). As shown in Fig. 2g, the normalized Co K-edge XANES of Ir-Co<sub>3</sub>O<sub>4</sub> clearly displays a slightly decreased valence state of the Co species induced by Ir incorporation. The corresponding Co K-edge EXAFS of Co<sub>3</sub>O<sub>4</sub> and Ir-Co<sub>3</sub>O<sub>4</sub> reveal three distinct peaks, identified as Co-O, octahedral Co-Co and tetrahedral Co-Co bonds, respectively<sup>51,52</sup>. However, a lower intensity of the Co-O and Co-Co bonds can be found in Ir-Co<sub>3</sub>O<sub>4</sub> in comparison with the Co<sub>3</sub>O<sub>4</sub>, indicating higher atomic chaos caused by introducing Ir atoms (Fig. 2h). The WT-EXAFS analysis on Co K-edge is consistent with the EXAFS results (Supplementary Fig. 10).

### Electrochemical performance of Ir-Co<sub>3</sub>O<sub>4</sub>

The OER performances of Ir-Co<sub>3</sub>O<sub>4</sub> and as-prepared Co<sub>3</sub>O<sub>4</sub> in 0.5 M H<sub>2</sub>SO<sub>4</sub> were investigated on glassy carbon electrode (GCE) together with the commercial IrO<sub>2</sub> and commercial Co<sub>3</sub>O<sub>4</sub> (denoted as IrO<sub>2</sub> and C-Co<sub>3</sub>O<sub>4</sub>, respectively) for comparison (Supplementary Fig. 11). All measured potentials in this study were calibrated to the reversible hydrogen electrode (RHE) scale (Supplementary Fig. 12). As shown in Supplementary Fig. 13, Ir-Co<sub>3</sub>O<sub>4</sub> exhibits a negatively shifted Co redox peak (III/IV) in the cyclic voltammetry (CV) curves compared to the Co<sub>3</sub>O<sub>4</sub>, indicating the isolated Ir sites can expedite the proton-electron transfer-mediated activation of Co to OER-active Co<sup>4+/3+</sup>. As expected, Ir-Co<sub>3</sub>O<sub>4</sub> exhibits the best OER performances among all studied samples. In terms of reaching the current density of 10 mA cm<sup>-2</sup>, Ir-Co<sub>3</sub>O<sub>4</sub> requires an overpotential ( $\eta$ ) of 236 mV, which is lower than that of Co<sub>3</sub>O<sub>4</sub> (412 mV) and C-Co<sub>3</sub>O<sub>4</sub> (511 mV). Notably, the low overpotential of Ir-Co<sub>3</sub>O<sub>4</sub> even suppresses that of benchmark IrO<sub>2</sub> (298 mV) with the same amounts of catalysts loading on electrode, as shown in Fig. 3a. Likewise, Ir-Co<sub>3</sub>O<sub>4</sub> displays the lowest onset potential among these catalysts, showing that it has the fastest OER activation rate (Supple-

mentary Fig. 14). The LSV curves of those catalysts without iR compensation are also displayed in Supplementary Fig. 15. In addition, the outstanding OER activity of Ir-Co<sub>3</sub>O<sub>4</sub> is also reflected by the smallest Tafel slope of 52.6 mV dec<sup>-1</sup> compared to that of IrO<sub>2</sub> (75.8 mV dec<sup>-1</sup>), Co<sub>3</sub>O<sub>4</sub> (109.8 mV dec<sup>-1</sup>) and C-Co<sub>3</sub>O<sub>4</sub> (131.3 mV dec<sup>-1</sup>), indicating that the OER kinetic of Ir-Co<sub>3</sub>O<sub>4</sub> is significantly accelerated (Fig. 3b). Corresponding graphs that plot the Tafel slope as a function of the overpotential on these catalysts are depicted in Supplementary Fig. 16, from which the boundary between kinetically-limited and mass transport limited currents can be clear distinguished. An obvious tendency of the boundary is followed as: Ir-Co<sub>3</sub>O<sub>4</sub> < IrO<sub>2</sub> < Co<sub>3</sub>O<sub>4</sub> < C-Co<sub>3</sub>O<sub>4</sub>. The evaluation of an electrocatalyst system is generally assessed by two key factors: specific activity and turnover frequency (TOF). The electrochemical active surface area (ECSA) was firstly estimated from the double-layer capacitance ( $C_{dl}$ ) measurements as shown in Supplementary Fig. 17<sup>54</sup>. By normalizing the OER current to ECSA at  $\eta$  = 300 mV, Ir-Co<sub>3</sub>O<sub>4</sub> shows the highest specific activity (0.098 mA cm<sup>-2</sup><sub>ECSA</sub>), almost 2.8 and 9.8 times higher than those of IrO<sub>2</sub> (0.035 mA cm<sup>-2</sup><sub>ECSA</sub>) and Co<sub>3</sub>O<sub>4</sub> (0.01 mA cm<sup>-2</sup><sub>ECSA</sub>). Moreover, Ir-Co<sub>3</sub>O<sub>4</sub> delivers a

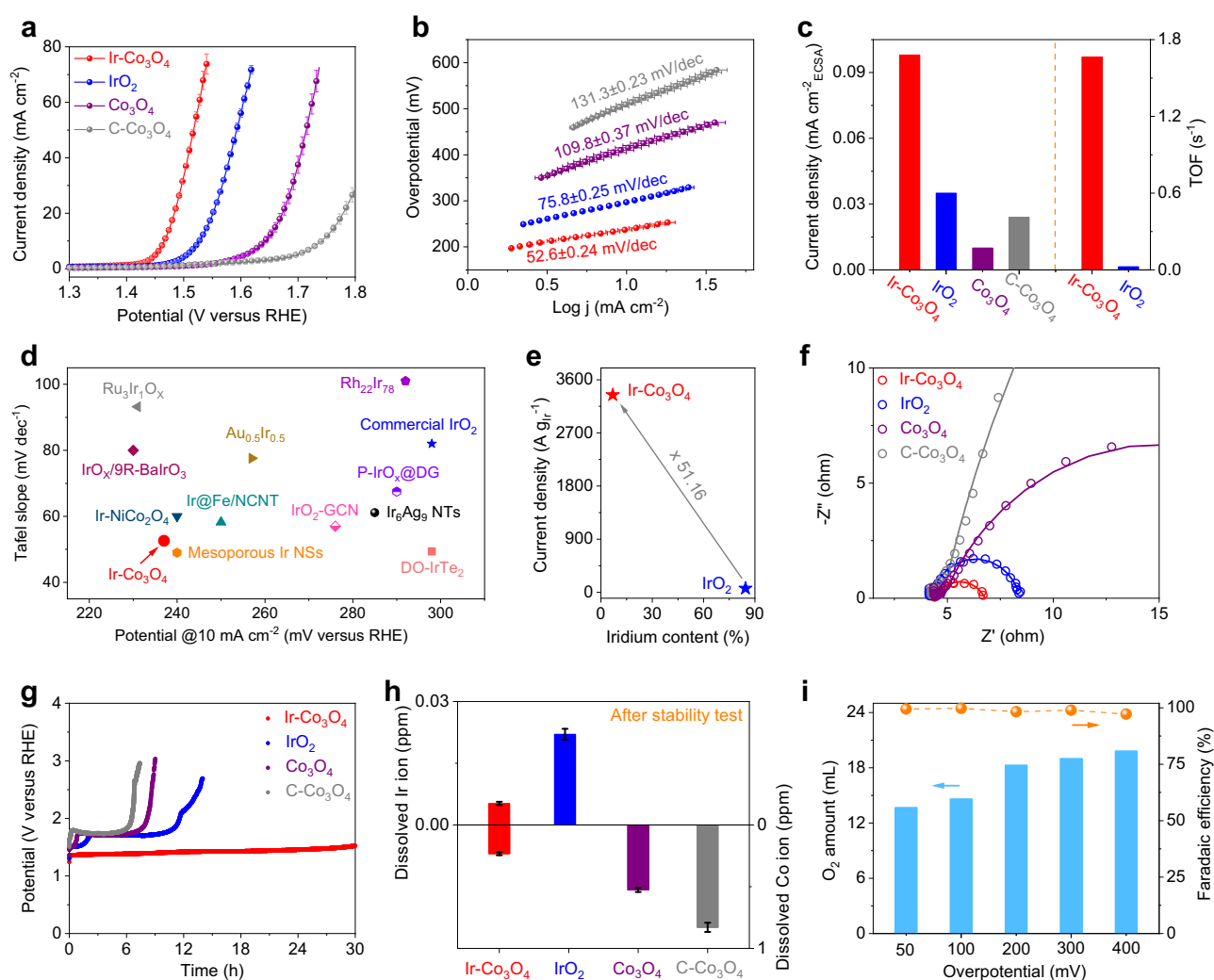


**Fig. 3 | Electrochemical OER of Ir-Co<sub>3</sub>O<sub>4</sub>.** **a** Polarization curves of Ir-Co<sub>3</sub>O<sub>4</sub>, IrO<sub>2</sub>, Co<sub>3</sub>O<sub>4</sub> and C-Co<sub>3</sub>O<sub>4</sub> in 0.5 M H<sub>2</sub>SO<sub>4</sub> at a scanning rate of 5 mV s<sup>-1</sup>. **b** Tafel plots derived from the polarization curves in (a). **c** Corresponding specific activities of Ir-Co<sub>3</sub>O<sub>4</sub>, IrO<sub>2</sub>, Co<sub>3</sub>O<sub>4</sub> and C-Co<sub>3</sub>O<sub>4</sub> at the overpotential of 300 mV. **d** Comparison of overpotentials and Tafel plots in reported Ir-based OER electrocatalysts. **e** Comparison of the mass activities normalized to Ir mass on Ir-Co<sub>3</sub>O<sub>4</sub> and IrO<sub>2</sub>. **f** EIS Nyquist plots and fitting curves of samples

recorded at the 1.43 V vs. RHE. **g** Chronopotentiometric measurements of Ir-Co<sub>3</sub>O<sub>4</sub>, IrO<sub>2</sub>, Co<sub>3</sub>O<sub>4</sub> and C-Co<sub>3</sub>O<sub>4</sub> at 10 mA cm<sup>-2</sup>, carbon paper was used as the catalyst support. **h** Dissolved Ir (left-y axis) and Co (right-y axis) ion concentrations measured for Ir-Co<sub>3</sub>O<sub>4</sub>, IrO<sub>2</sub>, Co<sub>3</sub>O<sub>4</sub> and C-Co<sub>3</sub>O<sub>4</sub> in the electrolyte by ICP-OES. **i** Generated O<sub>2</sub> amount and corresponding Faradaic efficiency over a range of overpotentials on Ir-Co<sub>3</sub>O<sub>4</sub>. Note: error bars represent the standard deviation of three independent measurements.

high intrinsic activity of TOF value normalized to Ir sites per geometric area of  $1.665 \text{ s}^{-1}$ , which is nearly 70-fold higher than that of  $\text{IrO}_2$  ( $0.0237 \text{ s}^{-1}$ ) (Fig. 3c). Also,  $\text{Ir-Co}_3\text{O}_4$  shows a higher TOF value than both  $\text{Co}_3\text{O}_4$  and  $\text{C-Co}_3\text{O}_4$  when normalized to Co sites per geometric area. In addition, ECSA-normalized TOF values further indicate the better intrinsic activity of  $\text{Ir-Co}_3\text{O}_4$  (Supplementary Fig. 18). BET-normalized specific activities were calculated to exclude the morphology effects on activity assessment, in which  $\text{Ir-Co}_3\text{O}_4$  also outperforms that of  $\text{Co}_3\text{O}_4$  (Supplementary Fig. 19). The above results confirm the incorporated Ir single atoms can efficiently boost the catalytic performances of Co spinel oxide beyond that of the noble  $\text{IrO}_2$ . A synopsis of previous literatures in Fig. 3d, highlights the merits of  $\text{Ir-Co}_3\text{O}_4$ , including low overpotential and Tafel slope are shown to be superior to most reported Ir-based OER electrocatalysts (Supplementary Table 4). In addition to the consideration of catalytic performance, cost-effectiveness is also of great significance for catalysts for practical applications. Thereafter the OER polarization currents of  $\text{Ir-Co}_3\text{O}_4$  and commercial  $\text{IrO}_2$  were normalized by the loading mass of Ir at  $\eta = 300 \text{ mV}$ . In addition, the mass activities were calculated from the LSV on carbon paper electrodes with higher electrode surface areas ( $1 \text{ cm}^2$ ) (Supplementary Fig. 20). As revealed in Fig. 3e, the mass activity of  $\text{Ir-Co}_3\text{O}_4$  is  $3343.37 \text{ A g}^{-1}_{\text{Ir}}$ , which is 51.16 times higher than that of  $\text{IrO}_2$  ( $65.35 \text{ A g}^{-1}_{\text{Ir}}$ ) at the overpotential of  $300 \text{ mV}$ . The superb mass activity derived from each Ir atoms indicates the remarkable economic efficiency of  $\text{Ir-Co}_3\text{O}_4$  towards OER. Electrochemical impedance spectroscopy (EIS) measurements of these four samples were tested under the same condition, as shown in Fig. 3f. In comparison with the charge transfer resistance ( $R_{\text{ct}}$ ) among  $\text{IrO}_2$  ( $4.18 \Omega$ ),  $\text{Co}_3\text{O}_4$  ( $20.55 \Omega$ ) and  $\text{C-Co}_3\text{O}_4$  ( $115.5 \Omega$ ),  $\text{Ir-Co}_3\text{O}_4$  displays the smallest  $R_{\text{ct}}$  of  $2.37 \Omega$  by establishing the equivalent circuit and fitting the Nyquist plots, implying that it has the lowest charge transfer resistance and the fastest charge transfer rate for the OER reaction (Supplementary Fig. 21 & Supplementary Table 5)<sup>55</sup>.

In addition to the activity, durability is another crucial criterion for the electrocatalytic performance of catalysts towards OER under operating conditions. As plotted in Fig. 3g,  $\text{Ir-Co}_3\text{O}_4$  shows long-term stability with a current density of  $10 \text{ mA cm}^{-2}$  for almost 30 h, which is superior to that of  $\text{IrO}_2$ ,  $\text{Co}_3\text{O}_4$  and  $\text{C-Co}_3\text{O}_4$  catalysts. Specifically, the commercial  $\text{IrO}_2$  and as-synthesized  $\text{Co}_3\text{O}_4$  can only maintain the current densities for nearly 15 h and 9 h, respectively, before they deactivate. CV scanning experiments further highlight that  $\text{Ir-Co}_3\text{O}_4$  exhibits a negligible increase of overpotential after 3000 cycles, whereas both  $\text{Co}_3\text{O}_4$  and  $\text{C-Co}_3\text{O}_4$  lost most of their activities (Supplementary Fig. 22). Both chronopotentiometric and CV scanning measurements demonstrate that the isolated Ir single sites enable activating the spinel Co oxide more durable in harsh OER environment. Further ICP-OES investigations show that leaching occurs preferentially at the Co species in  $\text{Ir-Co}_3\text{O}_4$ , but the dissolution effect of hosting  $\text{Co}_3\text{O}_4$  is alleviated by dispersed Ir single sites during OER reaction. In contrast,  $\text{IrO}_2$ ,  $\text{Co}_3\text{O}_4$  and  $\text{C-Co}_3\text{O}_4$  suffer from severe Ir and Co ions leaching after the OER durability test (Fig. 3h & Supplementary Fig. 23)<sup>56</sup>. The enhanced stability of  $\text{Ir-Co}_3\text{O}_4$  is induced by the doped effect of Ir single atoms, which is the main reason for the observed long-term stability in the acidic medium. In addition, the morphology characterizations by means of SEM and TEM reveal that  $\text{Ir-Co}_3\text{O}_4$  preserves the original ultrathin nanosheets with slight fractures after the chronopotentiometry at  $10 \text{ mA cm}^{-2}$ . No obvious structural changes can be found from the XRD pattern and HR-TEM images. Elemental mapping images show that Ir, Co and O elements are still homogeneously distributed over the entire  $\text{Ir-Co}_3\text{O}_4$  sample after OER (Supplementary Fig. 24). However, both the Ir 4f and Co 2p XPS spectra of post-OER  $\text{Ir-Co}_3\text{O}_4$  show increased valence states of Ir and Co, which is common for OER catalysts under oxidative voltages. The O 1s XPS binding energy of post-OER  $\text{Ir-Co}_3\text{O}_4$  shifts to a more positive position, further confirming the increase of valence state on overall catalyst

after the stability test (Supplementary Fig. 25). The stabilities of  $\text{Ir-Co}_3\text{O}_4$  and  $\text{IrO}_2$  were further tested at a higher current density of  $50 \text{ mA cm}^{-2}$ . As shown in Supplementary Fig. 26,  $\text{Ir-Co}_3\text{O}_4$  maintains the long-term stability up to 6 h, while  $\text{IrO}_2$  loses its activity after only 2 hours, further indicating the activity retention of  $\text{Ir-Co}_3\text{O}_4$  even at a high current density. On the other hand, complex OER is always accompanied with other side reactions such as catalyst/support oxidation, material dissolution and capacitive current effects, which may lead to the overestimation of actual activity and thus it is essential to estimate the associated OER Faradaic efficiency (FE) of the catalyst<sup>57</sup>. Gas chromatography (GC) was used to continuously monitor the generated  $\text{O}_2$  amount and calculate the FE on  $\text{Ir-Co}_3\text{O}_4$  over a wide range of overpotentials (Supplementary Fig. 27). As depicted in Fig. 3i, the corresponding  $\text{O}_2$  production increases with the increasing OER overpotentials; the calculated FE for OER remains at almost 100% at small overpotentials but drops slightly to 97% for large overpotentials. The relatively high FE values signify that the majority of energy is applied to drive OER and almost no side reactions occur on  $\text{Ir-Co}_3\text{O}_4$ . Overall, the high electrode/intrinsic activity and electrochemical durability conjointly endow  $\text{Ir-Co}_3\text{O}_4$  as a promising OER electrocatalyst candidate for practical applications in the acidic water electrolyzer, namely proton exchange membrane water electrolyzer. Going further, practical applications usually demand that the catalysts preparation process is contamination-free and non-toxic, as well as can easily realize gram-level preparation of catalysts in one batch<sup>58</sup>. Nevertheless, traditional synthesis methods for single-atom materials, including impregnation and solvothermal strategies usually require pollution-carrying organic solvent and their productions are seriously limited. For example, the similar atomic Ir-doped Co oxides have also been reported, but in which the multistep impregnation methods they employed can only prepare the electrocatalysts with milligram-level productions<sup>59,60</sup>. In contrast, the mechanochemical protocol we adopted for synthesizing  $\text{Ir-Co}_3\text{O}_4$  is environmental-friendly, adding only NaCl and NaOH for preparation besides metal precursors; the production can be readily scaled up to  $2.5 \text{ g}$  per batch. Resulting SEM, TEM, HR-TEM images, XRD pattern and SEM-EDS spectrum reveal no obvious structural and compositional changes on the mass-produced  $\text{Ir-Co}_3\text{O}_4$ . Elemental mappings show that Ir, Co and O are homogeneously distributed over the  $\text{Ir-Co}_3\text{O}_4$ . In addition, this mass-produced sample can largely maintain its original OER activity, demonstrating the potential of  $\text{Ir-Co}_3\text{O}_4$  for application in practical water electrolyzer (Supplementary Fig. 28).

### Mechanistic insights into OER process

Since the doped Ir single atoms promote the electrocatalytic performances of Co spinel oxide, the operando XANES tests at both Ir- $L_3$  edge and Co K-edge were carried out on  $\text{Ir-Co}_3\text{O}_4$  to learn more about the active sites and examine the chemical states evolution during the OER process. In the measurements, the operando XANES data were sequentially collected under the open circuit potential (OCP), one representative potential ( $1.6 \text{ V}$  vs. RHE) and then back to OCP again. Corresponding schematic diagram of the custom-built electrochemical cell and the obtained current-time (*i-t*) curves under applied voltages used for collecting the operando XAS data were depicted in Supplementary Fig. 29. As shown in Fig. 4a, the Ir- $L_3$  edge white line position at OCP shows a slight positive shift in energy as compared with that of fresh  $\text{Ir-Co}_3\text{O}_4$ , probably resulting from the delocalization of electron caused by adsorbed  $\text{H}_2\text{O}$  in the electrolyte. Upon increasing the applied voltage to  $1.6 \text{ V}$ , the peak position of Ir- $L_3$  shifts higher in energy by  $0.6 \text{ eV}$ , which suggests that isolated Ir atoms are evidently oxidized with an increased valence state during OER. In addition, the oxidized Ir atoms retain high chemical states even when the applied potential is reversed to OCP, indicating that the valence change is irreversible on  $\text{Ir-Co}_3\text{O}_4$  (Fig. 4c). As depicted in Supplementary Fig. 30, through further comparison of the white line position with standard

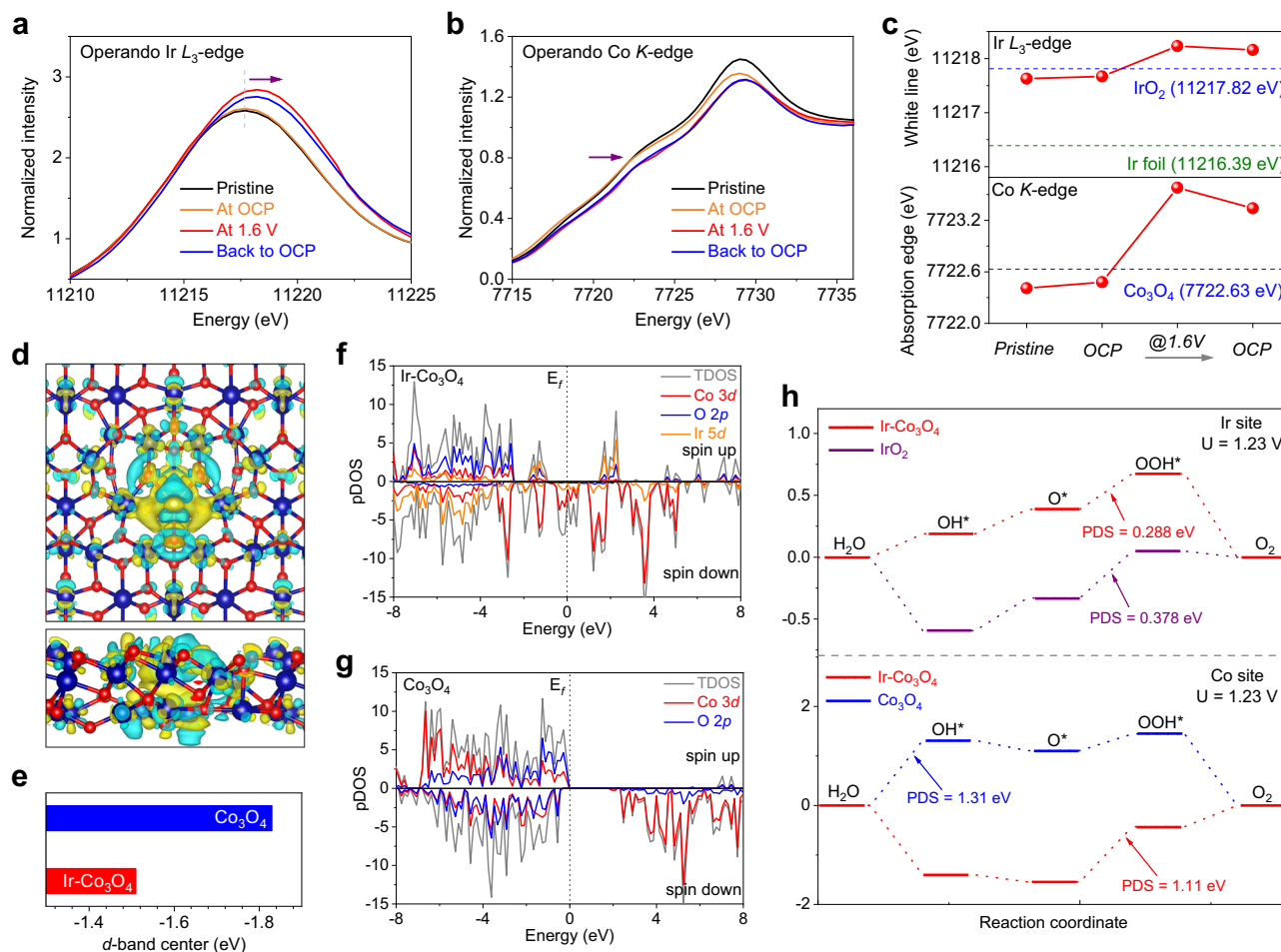


**Fig. 4 | Operando XANES analysis and energetic properties of Ir-Co<sub>3</sub>O<sub>4</sub> for OER.**

**a** The Ir L<sub>3</sub>-edge XANES and **(b)** the Co K-edge XANES of Ir-Co<sub>3</sub>O<sub>4</sub> measured in 0.5 M H<sub>2</sub>SO<sub>4</sub> under pristine state, OCP, OER operating condition of 1.6 V and OCP after OER operation. Ir L<sub>3</sub>-edge XANES of Ir foil and IrO<sub>2</sub>, and Co K-edge XANES of Co<sub>3</sub>O<sub>4</sub> are used as references. **c** The white line positions and the absorption edge positions

of all measured XANES. **d** The top and side panels of charge density difference on Ir-Co<sub>3</sub>O<sub>4</sub>. **e** Comparison of the *d*-band center of Ir-Co<sub>3</sub>O<sub>4</sub> and Co<sub>3</sub>O<sub>4</sub>. Corresponding Co 3d, O 2p and Ir 5d pDOS spectra of **(f)** Ir-Co<sub>3</sub>O<sub>4</sub> and **(g)** Co<sub>3</sub>O<sub>4</sub>. **h** The Gibbs free energy diagrams of the four-electron OER process on the Ir sites and Co sites of these catalysts under the applied overpotentials of 1.23 V vs. RHE, respectively.

references, it can be seen that the Ir-L<sub>3</sub> energy peak of Ir-Co<sub>3</sub>O<sub>4</sub> at the anodic potential of 1.6 V is located between the standard spectra of the Ir<sup>4+</sup> reference La<sub>2</sub>CoIrO<sub>6</sub> and the Ir<sup>5+</sup> reference Sr<sub>2</sub>CoIrO<sub>6</sub>, confirming it has a chemical state between +4 and +5. The average state of Ir single atoms is further estimated to be +4.46 according to the absorption energy-valence state standard curve<sup>26,48</sup>. In other words, there is a transition from Ir<sup>4+</sup> state to Ir<sup>4+</sup> state in part of the Ir-Co<sub>3</sub>O<sub>4</sub> catalysts during the electrochemical reactions. The phenomena discovered by operando XAS is definitely meaningful, as demonstrated by previous research showing that the Ir species with high valence state in combination with electrophilic O ligands act as the active sites of OER<sup>61,62</sup>. It is believed that the formed covalent Ir-O sites and electrophilic O ligands promote the O-O formation via a nucleophilic attack and thus support the enhanced OER performances. This suggests that the isolated Ir atoms are efficiently activated, endowing Ir-Co<sub>3</sub>O<sub>4</sub> with enhanced activity in OER<sup>63–66</sup>.

Subsequently, the valence change of Co species in Ir-Co<sub>3</sub>O<sub>4</sub> was also probed by operando Co K-edge XANES (Fig. 4b). As shown in Fig. 4c, the Co-K absorption edge of Ir-Co<sub>3</sub>O<sub>4</sub> at OCP is close to that of a Co<sub>3</sub>O<sub>4</sub> reference, but it gradually shifts to a higher energy by 1.0 eV under an applied voltage of 1.6 V, indicating an increase in the Co valence state by 0.47 through comparison with the standard references of Co<sup>2+</sup> reference (La<sub>2</sub>CoIrO<sub>6</sub>), Co<sup>3+</sup> reference (EuCoO<sub>3</sub>) and Co<sup>4+</sup> reference (BaCoO<sub>3</sub>) in Supplementary Fig. 31<sup>48</sup>. When the applied

voltage was set back to OCP, the Co species in Ir-Co<sub>3</sub>O<sub>4</sub> remain in the highly oxidized states. As a consequence, the continuously increased Ir and Co chemical states of Ir-Co<sub>3</sub>O<sub>4</sub> under operating voltages demonstrates that the both the Ir single atoms and Co atoms are functionalized as the OER active sites in Ir-Co<sub>3</sub>O<sub>4</sub>, which are responsible for charge transfer in catalytic reactions together.

To further understand the OER mechanism and the synergistic function on Ir-Co<sub>3</sub>O<sub>4</sub>, a theoretical study was performed based on density functional theory (DFT) calculations. As shown in Fig. 4d, the charge density difference on Ir-Co<sub>3</sub>O<sub>4</sub> indicates that the incorporation of Ir into Co<sub>3</sub>O<sub>4</sub> can effectively regulate the charge redistribution, where the Ir atom tends to lose electrons and the delocalized electrons accumulate around adjacent Ir-O bonds. This result also confirms a strong electronic interaction between the Ir single site and the host Co<sub>3</sub>O<sub>4</sub><sup>67</sup>. In addition, as shown in Fig. 4e it can be obtained that the *d*-band center position of Ir-Co<sub>3</sub>O<sub>4</sub> (−1.512 eV) is higher than that of Co<sub>3</sub>O<sub>4</sub> (−1.834 eV). The positive shift of *d*-band center would stabilize the interaction between the catalyst surface and the adsorbates, which is in strong alignment with the calculated free energy in Fig. 4h<sup>68</sup>. The projected density of states (pDOS) suggests that the introduction of Ir causes new hybridized electronic states in Ir-Co<sub>3</sub>O<sub>4</sub>, leading to a widening of the total density of states (TDOS) near the Fermi level, whereas the TDOS of Co<sub>3</sub>O<sub>4</sub> displays a band gap. The apparent difference demonstrates that the introduction of Ir single atoms endow



the  $\text{Co}_3\text{O}_4$  with metallic characters, leading to a better electronic conductivity than that of  $\text{Co}_3\text{O}_4$  for faster OER kinetics, which is consistent with our EIS measurements. Furthermore, the synergistic function between Ir atom and  $\text{Co}_3\text{O}_4$  was investigated by checking the Co  $3d$ , O  $2p$  and Ir  $5d$  pDOS, in which it can be clearly observed that the Ir  $5d$  orbit is substantially overlapped with Co  $2p$  orbit in pDOS, suggesting the strong interaction and more covalent character between Co and Ir atoms (Fig. 4f, g)<sup>26</sup>. In addition, the Gibbs free energy changes of acidic OER intermediates ( $\text{OH}^*$ ,  $\text{O}^*$ ,  $\text{OOH}^*$ ) in the elementary steps under the applied potential of 1.23 and 0 V vs. RHE are displayed in Fig. 4h and Supplementary Fig. 32, respectively. The potential determining steps (PDS) of Ir sites were first calculated and results reveal that the limiting steps occur at the conversion from  $\text{O}^*$  to  $\text{OOH}^*$  on both Ir- $\text{Co}_3\text{O}_4$  and  $\text{IrO}_2$ . Their corresponding PDS values are 0.288 eV and 0.378 eV, suggesting the lower energy barrier and better OER performance of Ir- $\text{Co}_3\text{O}_4$ . Furthermore, the calculations on Co sites indicate that the PDS on  $\text{Co}_3\text{O}_4$  is primarily derived from the transformation from  $\text{H}_2\text{O}$  to  $\text{OH}^*$  with an energy barrier of 1.31 eV. However, the PDS is changed as the formation of  $\text{OOH}^*$  and the corresponding energy barrier is further reduced to 1.11 eV on Ir- $\text{Co}_3\text{O}_4$ , emphasizing the promoting effect toward OER derived from Ir single sites<sup>29</sup>. It is believed that the electrophilic characters render these oxygen ligands caused by high-valence Ir susceptible to nucleophilic acid-base-type O-O bond formation at reduced kinetic barrier, leading to enhanced OER activity<sup>61,62</sup>. Therefore, both the operando XAS characterizations and DFT calculations conjointly demonstrate that the remarkable catalytic performance on Ir- $\text{Co}_3\text{O}_4$  is due to the synergistic cooperation between Ir and Co single sites with their bridged O ligands as well as the distinctly reduced energy barrier toward OER.

## Discussion

In conclusion, the active Ir- $\text{Co}_3\text{O}_4$  OER catalyst was successfully synthesized via a facile and economical mechanochemical method. Both AC HAADF-STEM characterization and XAS technique confirm that isolated Ir single atoms are homogeneously dispersed in the  $\text{Co}_3\text{O}_4$  host material. Consequently, OER measurement in acidic medium reveals that the overpotential of as-prepared  $\text{Co}_3\text{O}_4$  (412 mV) sharply decreases to 236 mV by doping a trace amount of Ir atoms, and its long-term stability is prolonged. Notably, the normalized mass activity and TOF of Ir- $\text{Co}_3\text{O}_4$  are higher than those of commercial  $\text{IrO}_2$ . By virtue of the operando XANES analysis, we recognize that the Ir single atoms are partially activated to higher valence under anodic voltages, simultaneously both Co and Ir atoms with their electrophilic O ligands served as active sites are synergistically responsible for charge transferring during OER process. DFT calculations further demonstrate the improved electronic conductivity and lower energy barrier towards OER by the electrophilic characters of oxygen ligands induced by high-valence Ir, boosting OER activity. Additionally, in contrast to most traditional synthesis methods for single-atom catalysts, which are limited to milligram-level production, the Ir- $\text{Co}_3\text{O}_4$  preparation can be easily scaled up to gram-level production with negligible activity loss. This study highlights the rational design of a promising, cost-effective and energy-efficient catalyst for boosting oxygen evolution in the acidic medium, and this prototype would potentially stimulate industrial interest in a larger scale for practical applications.

## Methods

### Materials

Iridium trichloride ( $\text{IrCl}_3$ , solid, 99.9%) was purchased from Ark Pharm. Cobalt chloride hexahydrate ( $\text{CoCl}_2 \cdot 6\text{H}_2\text{O}$ , solid, AR) was purchased from Aladdin. Sodium chloride ( $\text{NaCl}$ , solid, 99.8%) and sodium hydroxide ( $\text{NaOH}$ , solid, 97%) were purchased from Sinopharm Chemical Reagent Co. Ltd (Shanghai, China). Cobalt oxide ( $\text{Co}_3\text{O}_4$ , solid, 99.7%) was purchased from Alfa Aesar. Iridium oxide ( $\text{IrO}_2$ , solid, 99.9%) was purchased from Innochem. Isopropanol ( $\text{C}_3\text{H}_8\text{O}$ , liquid,  $\geq$

99.7%) and sulfuric acid ( $\text{H}_2\text{SO}_4$ , liquid,  $\geq 96\%$ ) were purchased from Sinopharm Chemical Reagent Co. Ltd (Shanghai, China).

### Catalyst synthesis

The preparation of Ir- $\text{Co}_3\text{O}_4$  was based on mechanochemical method. In a typical synthesis, 475.9 mg  $\text{CoCl}_2 \cdot 6\text{H}_2\text{O}$  (2 mmol) and 29.9 mg  $\text{IrCl}_3$  (0.1 mmol) were initially mixed in agate mortar for 5 min. Afterwards, 0.5 g  $\text{NaCl}$  was added into the evenly mixed precursors and ground for 10 min. A homogeneous powder was obtained and then put into a high-energy milling pot (Planetary Mono Mill, Pulverisette 6, Fritsch) with stainless steel balls for grinding for 1 h under a rotation speed of 500 rpm. After the first milling, 1 mL  $\text{NaOH}$  solution ( $5 \text{ mmol L}^{-1}$ ) was added into the above mixture and ball milling was continued for 1 h. Finally, the obtained slurry was collected from the milling pot and dried at 60 °C in an oven under air atmosphere, then it was calcined in air at 350 °C for 6 h with a heating rate of  $5 \text{ }^\circ\text{C s}^{-1}$ . After calcination, the sample was washed by water 3 times and dried overnight at 80 °C. The as-synthesized  $\text{Co}_3\text{O}_4$  was prepared by a similar method as Ir- $\text{Co}_3\text{O}_4$ , except that  $\text{IrCl}_3$  was not added as a precursor.

### Scale-up synthesis

To realize the mass production of Ir- $\text{Co}_3\text{O}_4$ , 2855.4 mg  $\text{CoCl}_2 \cdot 6\text{H}_2\text{O}$  (12 mmol) and 179.4 mg  $\text{IrCl}_3$  (0.6 mmol) were initially mixed in agate mortar for 20 min. Afterwards, 3.0 g  $\text{NaCl}$  was added into the evenly mixed precursors and ground for 20 min. The homogeneous powder was obtained and then put into the high-energy milling pot with stainless steel balls and ground for 3 h at a rotation speed of 500 rpm. After the first milling, 6 mL  $\text{NaOH}$  solution ( $5 \text{ mmol L}^{-1}$ ) was added into the above mixture and ball milling was continued for 3 h. Finally, the obtained slurry was collected from the milling pot and then calcined in air at 350 °C for 6 h at a heating rate of  $5 \text{ }^\circ\text{C s}^{-1}$ . After calcination, the sample was washed by water 3 times and dried overnight at 80 °C.

### Characterization

Scanning electron microscopy (SEM) images were collected on a Zeiss Supra 55 at an acceleration voltage of 5 kV. Transmission electron microscopy (TEM) and High-resolution TEM (HR-TEM) images were determined by a JEOL 2100F instrument at a working voltage of 200 kV. The aberration-corrected high angle annular dark field-scanning TEM (AC HAADF-STEM) images and corresponding elemental mapping were collected on an aberration correction Hitachi 2700D microscope operated at 200 kV. The  $\text{N}_2$  absorption/desorption isotherms were tested on a Autosorb iQ Quantachrome device and the specific surface area with pore distribution were obtained by the Brunauer–Emmett–Teller (BET) analysis. The mass fraction of Ir in Ir- $\text{Co}_3\text{O}_4$  and the dissolved ion concentrations after stability tests were determined by ICP-OES on an Agilent ICP-OES 730. The amount of  $\text{O}_2$  generated over a range of overpotentials were recorded by Agilent 7890B equipped with a  $5 \text{ \AA}$  molecular sieve column thermal conductivity detector; Ar was used as the carrier gas.

The electronic structure was investigated by XPS on a Thermo Scientific Escalab 250Xi with an Al- $\text{K}_\alpha$  source. XAS of Co  $K$ -edge and Ir  $L_3$ -edge were carried out at the 17C beamline at the National Synchrotron Radiation Research Center (NSRRC) in Taiwan. The operando XAS experiments of Co  $K$ -edge and Ir  $L_3$ -edge were performed at the 17C beamline at the NSRRC with a custom-built operando XAS instruments, corresponding data was collected by applying the constant voltage on the catalyst and the electrochemical bias was controlled as 1.6 V vs. RHE. All XAS experiments were carried out in ambient air under room temperature and analyzed using the standard program Demeter. For wavelet-transformed  $k^3$ -weighted EXAFS, the  $\chi(k)$  exported from Athena was imported into the Hama Fortran code designed by Harald Funke and Marina Chukalina. The parameters were listed as follows: R range, 0–6 Å, k range, 0–15 Å<sup>-1</sup>; k weight, 0; and



Morlet function with  $\kappa_{\text{Morlet}} = 10$ ,  $\sigma_{\text{Morlet}} = 1$  was used as the mother wavelet to provide the overall distribution.

The structure was analyzed by XRD with a Bruker D8 Advance powder diffractometer (operating at 40 kV, 40 mA) equipped with a  $\text{Cu-K}\alpha$  source ( $\lambda_1 = 1.5405 \text{ \AA}$ ,  $\lambda_2 = 1.5443 \text{ \AA}$ ) and fitted with a beryllium window at room temperature. Rietveld refinements for XRD data were carried out with the Full-Profit program, and the refined parameters were background parameters, line shift errors (zero shift), Caglioti coefficients (U, V and W), scale factor, lattice parameters, atomic position, atomic rate occupancy and isotropic atomic displacement parameters.

### Electrochemical measurement

The OER activity measurements in  $\text{O}_2$ -saturated  $0.5 \text{ M H}_2\text{SO}_4$  were performed at room temperature on a CHI 760E electrochemistry workstation with a rotating disk electrode (RDE) configuration (Pine Research Instrumentation) via using a standard three-electrode electrochemical cell. A glassy carbon (GC) electrode ( $0.196 \text{ cm}^2$ ), calomel electrode and graphite rod were used as the working, reference and counter electrode, respectively. Prior to each testing, the working electrode was ground and polished three times by fine aluminum oxide powder and washed with distilled water to remove the residual catalyst. The counter electrode was also cleaned by distilled water before being used. Before the electrocatalytic tests, samples (5 mg), carbon black (5 mg, Vulcan XC-72R) and 5 wt% Nafion solution (0.1 mL, Aldrich) were dispersed in absolute isopropanol (1.9 mL) via mild sonication to produce a homogeneous catalysts ink. Then, 20  $\mu\text{L}$  of the catalyst ink was dropped onto the GC electrode with a diameter of 0.5 cm and dried under infrared light. The active materials that dropped on the electrode were 50 wt%. Metal mass loadings on the electrode for all samples were controlled at  $0.255 \text{ mg cm}^{-2}$ . The Ir mass loadings for  $\text{Ir-Co}_3\text{O}_4$  and  $\text{IrO}_2$  were calculated to be  $0.018 \text{ mg cm}^{-2}$  and  $0.218 \text{ mg cm}^{-2}$ , respectively. The Co mass loadings for  $\text{Ir-Co}_3\text{O}_4$ ,  $\text{Co}_3\text{O}_4$  and  $\text{C-Co}_3\text{O}_4$  were calculated to be  $0.174 \text{ mg cm}^{-2}$ ,  $0.187 \text{ mg cm}^{-2}$  and  $0.187 \text{ mg cm}^{-2}$ , respectively. All OER potentials were calibrated with respect to RHE scale (Supplementary Fig. 12). The calibration was performed by using a Pt wire as the working electrode, the calomel electrode as the reference electrode and a graphite rod as the counter electrode in a  $\text{H}_2$ -saturated electrolyte ( $0.5 \text{ M H}_2\text{SO}_4$ ). Linear sweep voltammetry (LSV) was carried out with a scan rate of  $1 \text{ mV s}^{-1}$  and the potential at which the current crossed zero was the calibration value. Cyclic voltammetry (CV) scans were initially performed at the scan rate of  $100 \text{ mV s}^{-1}$  between 1.1 and 1.5 V (vs. RHE) with no iR compensation for 50 cycles to activate and clean the catalyst surfaces. Subsequently, LSV with iR correction was conducted at a scan rate of  $5 \text{ mV s}^{-1}$  under room temperature to test the OER activity. The iR correction was automatic compensation by the used electrochemical workstation and was controlled as 95% rather than 100% to prevent the resonance and large data error. Tafel slopes were probed on  $\text{Ir-Co}_3\text{O}_4$ ,  $\text{IrO}_2$ ,  $\text{Co}_3\text{O}_4$  and  $\text{C-Co}_3\text{O}_4$  within the potential range of 1.43–1.48 V vs. RHE, 1.48–1.56 V vs. RHE, 1.58–1.7 V vs. RHE and 1.69–1.81 V vs. RHE, respectively. And the Tafel slopes were determined by plotting the overpotential vs. the logarithm of current density ( $\log |j|$ ). Stability was evaluated using catalysts loaded carbon paper ( $1 \text{ cm}^2$ ) with mass loadings of  $0.255 \text{ mg cm}^{-2}$  to carry out chronopotentiometry at a constant OER current density of  $10 \text{ mA cm}^{-2}$ . Cyclic stability tests on  $\text{Ir-Co}_3\text{O}_4$ ,  $\text{IrO}_2$ ,  $\text{Co}_3\text{O}_4$  and  $\text{C-Co}_3\text{O}_4$  were performed under room temperature within the potential range of 1.1–1.5 V vs. RHE, 1.16–1.56 V vs. RHE, 1.28–1.68 V vs. RHE and 1.38–1.78 V vs. RHE for 3000 cycles, respectively. All scan rates were controlled as  $100 \text{ mV s}^{-1}$ . Electrochemical impedance spectroscopy was measured on the Bio-Logic SP-200 workstation in the frequency range of 0.01–100 kHz at the 1.43 V vs. RHE; a corresponding equivalent circuit and fitting resistance value were analyzed by EC-lab Software Analysis.

### Calculation of the electrochemically surface area

The electrochemically active surface area (ECSA) for also catalysts was estimated from the electrochemical double-layer capacitance ( $C_{\text{dl}}$ ) of the catalytic surface according to Eq. (1):

$$\text{ECSA} = R_f S = \frac{C_{\text{dl}}}{C_s} S \quad (1)$$

where  $C_{\text{dl}}$  was measured from the scan-rate-dependent CVs in the non-Faradaic region of 0.75–0.95 V vs. RHE in  $0.5 \text{ M H}_2\text{SO}_4$  with scan rates of 20, 40, 60, 80 and  $100 \text{ mV s}^{-1}$ . The units for  $R_f$  and  $S$  are  $\text{cm}^2_{\text{real}}$  and  $\text{cm}^2_{\text{geo}}$ , respectively.  $S$  stands for the real surface area of the smooth metal electrode, which was generally equal to the geometric area of the glassy carbon electrode ( $S = 0.196 \text{ cm}^2$ ). The specific capacitance ( $C_s$ ) for a flat surface was found to be in the range of 20–60  $\mu\text{F cm}^{-2}$ . In this work, a  $C_s$  value of  $60 \mu\text{F cm}^{-2}$  was used to estimate the ECSA.

### Calculation of the turnover frequency

The turnover frequency (TOF) of these catalysts was calculated using Eq. (2):

$$\text{TOF} = \frac{\text{\#number of total oxygen turnover}/\text{cm}^2_{\text{geo}}}{\text{\#number of active sites}/\text{cm}^2_{\text{geo}}} \quad (2)$$

the  $\text{O}_2$  turnover per geometric area was obtained from the geometric current density for the LSV curves according to Eq. (3):

$$\text{O}_2 \text{ turnover per geometric area} = j_{\text{geo}} \times \frac{1 \text{ Cs}^{-1}}{1000 \text{ mA}} \times \frac{1 \text{ mol}}{96485.3 \text{ C}} \times \frac{1}{4} \times \frac{6.02 \times 10^{23}}{1 \text{ mol O}_2} \quad (3)$$

the number of the active sites per geometric area can be calculated from the results of the ICP-AES analysis. For example, the upper limit of Ir site density of  $\text{Ir-Co}_3\text{O}_4$  is:

$$0.05 \text{ mg} \times 6.9\% \times \frac{1 \text{ mmol}}{192.2 \text{ mg}} \times \frac{6.02 \times 10^{20} \text{ sites}}{1 \text{ mmol}} \times \frac{1}{0.196 \text{ cm}^2} = 5.51 \times 10^{16} \text{ sites cm}^{-2}$$

At the overpotential of 300 mV, the OER current density for  $\text{Ir-Co}_3\text{O}_4$  is  $58.84 \text{ mA cm}^{-2}$ . And the corresponding TOF value normalized to geometric area was calculated to be:

$$\text{TOF}_{\text{geo}} = \frac{1.56 \times 10^{15} \frac{\text{O}_2}{\text{cm}^2} \text{ s}^{-1} \text{ per } \frac{\text{mA}}{\text{cm}^2} \times 58.84 \frac{\text{mA}}{\text{cm}^2}}{5.51 \times 10^{16} \frac{\text{site}}{\text{cm}^2}} = 1.665 \text{ s}^{-1}$$

In addition, the  $\text{O}_2$  turnover per ECSA was obtained according to Eq. (4):

$$\text{TOF}_{\text{ECSA}} = \frac{\text{\#number of total oxygen turnover} \times \text{absolult value of current density}}{\text{\#active sites} \times \text{ECSA}} \quad (4)$$

Thus the corresponding TOF value of  $\text{Ir-Co}_3\text{O}_4$  normalized to ECSA polarization information was calculated to be:

$$\text{TOF}_{\text{ECSA}} = \frac{1.56 \times 10^{15} \frac{\text{O}_2}{\text{cm}^2} \text{ s}^{-1} \text{ per } \frac{\text{mA}}{\text{cm}^2} \times 58.84 \frac{\text{mA}}{\text{cm}^2}}{5.51 \times 10^{16} \frac{\text{site}}{\text{cm}^2} \times 125.9 \text{ cm}^2} = 0.0132 \text{ s}^{-1}$$

The TOF per metal site is calculated based hypothesis that all Ir or all Co atoms are accessible to the electrolyte in all cases. Other catalysts were calculated according to the same procedure.

### Calculation of OER Faradaic efficiency

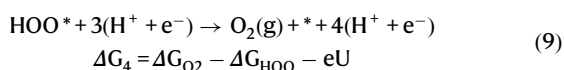
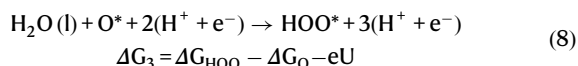
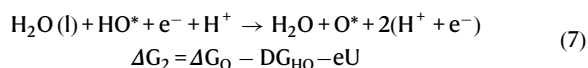
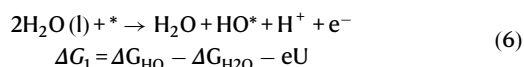
The amount of produced  $O_2$  was tested for Ir-Co<sub>3</sub>O<sub>4</sub> dropped carbon paper with a mass loading of 0.255 mg cm<sup>-2</sup> as the working electrode to conduct OER in a sealed cell. The applied potentials on sample to generated  $O_2$  were 1.28 V, 1.33 V, 1.43 V, 1.53 V and 1.63 V vs. RHE, respectively. Then Ar was used as the carrier gas to purge the produced  $O_2$  into a gas chromatograph (Agilent 7890B) equipped with a 5 Å molecular sieve column thermal conductivity detector to generate the  $O_2$  signal peak. By fitting the relationship between a certain amount of  $O_2$  and the corresponding GC  $O_2$  signal area, a standard curve was established. By transforming the generated  $O_2$  peak area at different overpotentials into the standard curve, the generated  $O_2$  amounts on Ir-Co<sub>3</sub>O<sub>4</sub> were calculated. The OER Faradaic efficiency (FE) of Ir-Co<sub>3</sub>O<sub>4</sub> was obtained according to:

$$FE = \frac{neF}{Q} \quad (5)$$

where  $e$  is the number of electrons transferred for generating  $O_2$ ,  $Q$  is the total charge,  $n$  is the amount of generated  $O_2$  (in moles) and  $F$  is the Faradaic constant.

### Computational details

The geometries and energies were performed by the density functional theory (DFT) calculations with the Vienna Ab-initio Simulation Package (VASP)<sup>69,70</sup>. The interactions between ion cores and valence electrons were described by projector augmented wave (PAW) method<sup>71</sup>. The exchange correlation interaction was described with the generalized gradient approximation (GGA) with the Perdew-Burke-Ernzerhof (PBE) functional<sup>72</sup>. Dispersion correction (DFT-D3) was considered in all energy-related calculations. The wave functions at each k-point were expanded with a plane wave basis set with a kinetic cutoff energy of 400 eV. Geometries were optimized using a force-based conjugate-gradient method until the energy was converged to  $1.0 \times 10^{-7}$  eV/atom and the force to 0.02 eV/Å. The Brillouin zone was sampled with a  $3 \times 4 \times 1$  Monkhorst-Pack k-point mesh. The optimized (111) plane was adopted as the model for surface reaction pathways. Co<sub>3</sub>O<sub>4</sub> (111) was constructed by cutting the bulk Co<sub>3</sub>O<sub>4</sub> along 111 directions. Ir doped Co<sub>3</sub>O<sub>4</sub> was prepared by replacing one Co atom on the surface. During the optimization the up-layer atoms were allowed to relax and the atoms in the bottom layer were fixed to match the bulk structure. A vacuum layer of 15 Å was used along the  $c$  direction normal to the surface to avoid periodic interactions. The pDOS calculations were taken from the bare surfaces of studied samples and were calculated by hybrid functional HSE06 for the accuracy of electron distribution<sup>73</sup>. The  $d$ -band center was extracted from the average of the integral of  $d$ -band pDOS information. The Gibbs free energy was calculated based on the four-electron OER mechanism proposed by Nørskov<sup>16</sup>, corresponding formulas are listed as:



Both free energy profiles were calculated on the Ir and Co sites in samples, respectively. The applied overpotentials were set as 0 and 1.23 V vs. RHE, respectively. Free energy diagrams were estimated as  $\Delta G = \Delta E + \Delta ZPE - T\Delta S$ , where  $E$ ,  $ZPE$ ,  $T$ , and  $S$  are the total energy obtained from DFT calculations, the zero-point energy (ZPE), the temperature (298.15 K), the entropy obtained from vibrational frequency calculations, respectively<sup>74,75</sup>. In addition, the frequencies were set to be 50 cm<sup>-1</sup>.

### Data availability

All relevant data are available from the corresponding authors on request. Source data are provided with this paper.

### References

1. Chu, S. & Majumdar, A. Opportunities and challenges for a sustainable energy future. *Nature* **488**, 294–303 (2012).
2. Smalley, R. E. Future global energy prosperity: the terawatt challenge. *MRS Bull.* **30**, 412–417 (2011).
3. Seitz, L. C. et al. A highly active and stable IrO<sub>x</sub>/SrIrO<sub>3</sub> catalyst for the oxygen evolution reaction. *Science* **353**, 1011–1014 (2016).
4. King, L. A. et al. A non-precious metal hydrogen catalyst in a commercial polymer electrolyte membrane electrolyser. *Nat. Nanotechnol.* **14**, 1071–1074 (2019).
5. Koper, M. T. M. Theory of multiple proton-electron transfer reactions and its implications for electrocatalysis. *Chem. Sci.* **4**, 2710–2723 (2013).
6. Reier, T., Nong, H. N., Teschner, D., Schlögl, R. & Strasser, P. Electrocatalytic oxygen evolution reaction in acidic environments – reaction mechanisms and catalysts. *Adv. Energy Mater.* **7**, 1601275 (2017).
7. Shan, J. et al. Charge-redistribution-enhanced nanocrystalline Ru@IrO<sub>x</sub> electrocatalysts for oxygen evolution in acidic media. *Chem* **5**, 445–459 (2019).
8. Zhang, Z. et al. Selectively anchoring single atoms on specific sites of supports for improved oxygen evolution. *Nat. Commun.* **13**, 2473 (2022).
9. Meng, G. et al. Strain regulation to optimize the acidic water oxidation performance of atomic layer IrO<sub>x</sub>. *Adv. Mater.* **31**, 1903616 (2019).
10. Wang, J. et al. Exceptionally active and stable RuO<sub>2</sub> with interstitial carbon for water oxidation in acid. *Chem* **8**, 1673–1687 (2022).
11. Xiao, Z. et al. Operando identification of the dynamic behavior of oxygen vacancy-rich Co<sub>3</sub>O<sub>4</sub> for oxygen evolution reaction. *J. Am. Chem. Soc.* **142**, 12087–12095 (2020).
12. Liu, Z. et al. Optimal geometrical configuration of cobalt cations in spinel oxides to promote oxygen evolution reactions. *Angew. Chem. Int. Ed. Engl.* **59**, 4736–4742 (2020).
13. Wu, Y. et al. Electron density modulation of NiCo<sub>2</sub>S nanowires by nitrogen incorporation for highly efficient hydrogen evolution catalysis. *Nat. Commun.* **9**, 1425 (2018).
14. Huang, Z.-F. et al. Chemical and structural origin of lattice oxygen oxidation in Co-Zn oxyhydroxide oxygen evolution electrocatalysts. *Nat. Energy* **4**, 329–338 (2019).
15. Wang, J. et al. Redirecting dynamic surface restructuring of a layered transition metal oxide catalyst for superior water oxidation. *Nat. Catal.* **4**, 212–222 (2021).
16. Man, I. C. et al. Universality in oxygen evolution electrocatalysis on oxide surfaces. *ChemCatChem* **3**, 1159–1165 (2011).
17. Blasco-Ahicart, M., Soriano-López, J., Carbó, J. J., Poblet, J. M. & Galan-Mascaros, J. R. Polyoxometalate electrocatalysts based on Earth-abundant metals for efficient water oxidation in acidic media. *Nat. Chem.* **10**, 24–30 (2017).
18. Yuan, X. et al. Controlled phase evolution from Co nanochains to CoO nanocubes and their application as OER catalysts. *ACS Energy Lett.* **2**, 1208–1213 (2017).

19. Li, A. et al. Enhancing the stability of cobalt spinel oxide towards sustainable oxygen evolution in acid. *Nat. Catal.* **5**, 109–118 (2022).
20. Jiao, F. & Frei, H. Nanostructured cobalt oxide clusters in mesoporous silica as efficient oxygen-evolving catalysts. *Angew. Chem. Int. Ed.* **48**, 1841–1844 (2009).
21. Zhang, L. et al. Facet dependent oxygen evolution activity of spinel cobalt oxides. *J. Electrochem.* **28**, 2108481 (2022).
22. Huynh, M., Ozel, T., Liu, C., Lau, E. C. & Nocera, D. G. Design of template-stabilized active and Earth-abundant oxygen evolution catalysts in acid. *Chem. Sci.* **8**, 4779–4794 (2017).
23. Song, J. et al. A review on fundamentals for designing oxygen evolution electrocatalysts. *Chem. Soc. Rev.* **49**, 2196–2214 (2020).
24. Zhang, B. et al. Homogeneously dispersed multimetal oxygen-evolving catalysts. *Science* **352**, 333–337 (2016).
25. Zhang, J. et al. Single-atom Au/NiFe layered double hydroxide electrocatalyst: probing the origin of activity for oxygen evolution reaction. *J. Am. Chem. Soc.* **140**, 3876–3879 (2018).
26. Li, L. et al. In situ/operando capturing unusual Ir<sup>6+</sup> facilitating ultrafast electrocatalytic water oxidation. *Adv. Funct. Mater.* **31**, 2104746 (2021).
27. Pi, Y., Shao, Q., Wang, P., Guo, J. & Huang, X. General formation of monodisperse IrM (M = Ni, Co, Fe) bimetallic nanoclusters as bifunctional electrocatalysts for acidic over water splitting. *Adv. Funct. Mater.* **27**, 1700886 (2017).
28. Shah, K. et al. Cobalt single atom incorporated in ruthenium oxide sphere: a robust bifunctional electrocatalyst for HER and OER. *Angew. Chem. Int. Ed.* **61**, e202114951 (2022).
29. Qiao, B. et al. Single-atom catalysis of CO oxidation using Pt<sub>1</sub>/FeO<sub>x</sub>. *Nat. Chem.* **3**, 634–641 (2011).
30. Zhang, J. et al. Single platinum atoms immobilized on an MXene as an efficient catalyst for the hydrogen evolution reaction. *Nat. Catal.* **1**, 985–992 (2018).
31. Jiang, K. et al. Single platinum atoms embedded in nanoporous cobalt selenide as electrocatalyst for accelerating hydrogen evolution reaction. *Nat. Commun.* **10**, 1743 (2019).
32. Jiang, K. et al. Isolated Ni single atoms in graphene nanosheets for high-performance CO<sub>2</sub> reduction. *Energy Environ. Sci.* **11**, 893–903 (2018).
33. Mao, J. et al. Accelerating water dissociation kinetics by isolating cobalt atoms into ruthenium lattice. *Nat. Commun.* **9**, 4958 (2018).
34. Yan, Q.-Q. et al. Reversing the charge transfer between platinum and sulfur-doped carbon support for electrocatalytic hydrogen evolution. *Nat. Commun.* **10**, 4977 (2019).
35. Luo, Z. et al. Chemically activating MoS<sub>2</sub> via spontaneous atomic palladium interfacial doping towards efficient hydrogen evolution. *Nat. Commun.* **9**, 2120 (2018).
36. Hai, X. et al. Scalable two-step annealing method for preparing ultra-high-density single-atom catalyst libraries. *Nat. Nanotechnol.* **17**, 174–181 (2022).
37. Zhao, Z. et al. Boosting the oxygen evolution reaction using defect-rich ultra-thin ruthenium oxide nanosheets in acidic media. *Energy Environ. Sci.* **13**, 5143–5151 (2020).
38. Cao, K. et al. Efficient direct H<sub>2</sub>O<sub>2</sub> synthesis enabled by PdPb nanorings via inhibiting the O–O bond cleavage in O<sub>2</sub> and H<sub>2</sub>O<sub>2</sub>. *ACS Catal.* **11**, 1106–1118 (2021).
39. Zhang, Y. et al. Atomic iridium incorporated in cobalt hydroxide for efficient oxygen evolution catalysis in neutral electrolyte. *Adv. Mater.* **30**, 1707522 (2018).
40. Pfeifer, V. et al. The electronic structure of iridium oxide electrodes active in water splitting. *Phys. Chem. Chem. Phys.* **18**, 2292 (2016).
41. Pfeifer, V. et al. The electronic structure of iridium and its oxides. *Surf. Interface Anal.* **48**, 261–273 (2016).
42. Pfeifer, V. et al. In situ observation of reactive oxygen species forming on oxygen-evolving iridium surfaces. *Chem. Sci.* **8**, 2143–2149 (2017).
43. Li, P. et al. Boosting oxygen evolution of single-atomic ruthenium through electronic coupling with cobalt-iron layered double hydroxides. *Nat. Commun.* **10**, 1711 (2019).
44. Baroudi, K. et al. Structure and properties of α-NaFeO<sub>2</sub>-type ternary sodium iridates. *J. Solid. State Chem.* **210**, 195–205 (2014).
45. Deng, H. et al. Strong enhancement of spin ordering by A-site magnetic ions in the ferrimagnet CaCu<sub>3</sub>Fe<sub>2</sub>O<sub>8</sub>. *Phys. Rev. B* **94**, 024414 (2016).
46. Feng, H. et al. Ba<sub>2</sub>NiOsO<sub>6</sub>: A Dirac-Mott insulator with ferromagnetism near 100 K. *Phys. Rev. B* **94**, 235158 (2016).
47. Feng, H. et al. Room-temperature ferrimagnetism of anti-site-disordered Ca<sub>2</sub>MnOsO<sub>6</sub>. *Phys. Rev. Mater.* **3**, 124404 (2019).
48. Agrestini, S. et al. Nature of the magnetism of iridium in the double perovskite Sr<sub>2</sub>CoIrO<sub>6</sub>. *Phys. Rev. B* **100**, 014443 (2019).
49. Guan, D. et al. Exceptionally robust face-sharing motifs enable efficient and durable water oxidation. *Adv. Mater.* **33**, 2103392 (2021).
50. Chen, G. et al. Ultrahigh-performance tungsten-doped perovskites for the oxygen evolution reaction. *J. Mater. Chem. A* **6**, 9854–9859 (2018).
51. Liu, H. et al. Insight into the role of metal–oxygen bond and O 2p hole in high-voltage cathode LiNi<sub>x</sub>Mn<sub>2–x</sub>O<sub>4</sub>. *J. Phys. Chem. C* **121**, 16079–16087 (2017).
52. Guan, D. et al. Utilizing ion leaching effects for achieving high oxygen-evolving performance on hybrid nanocomposite with self-optimized behaviors. *Nat. Commun.* **11**, 3376 (2020).
53. Dai, Y. et al. Bridging the charge accumulation and high reaction order for high-rate oxygen evolution and long stable Zn-air batteries. *Adv. Funct. Mater.* **32**, 2111989 (2022).
54. Guan, D. et al. Screening highly active perovskites for hydrogen-evolving reaction via unifying ionic electronegativity descriptor. *Nat. Commun.* **10**, 3755 (2019).
55. Li, G. et al. The synergistic effect of Hf–O–Ru bonds and oxygen vacancies in Ru/HfO<sub>2</sub> for enhanced hydrogen evolution. *Nat. Commun.* **13**, 1270 (2022).
56. Shi, Z. et al. Confined Ir single sites with triggered lattice oxygen redox: toward boosted and sustained water oxidation catalysis. *Joule* **5**, 2164–2176 (2021).
57. Zheng, Y.-R. et al. Monitoring oxygen production on mass-selected iridium–tantalum oxide electrocatalyst. *Nat. Energy* **7**, 55–64 (2022).
58. Xiong, Y. et al. Gram-scale synthesis of high-loading single-atomic-site Fe catalysts for effective epoxidation of styrene. *Adv. Mater.* **32**, 2000896 (2020).
59. Lu, Y. et al. Tuning the selective adsorption site of biomass on Co<sub>3</sub>O<sub>4</sub> by Ir single atoms for electrosynthesis. *Adv. Mater.* **33**, 2007056 (2021).
60. Shan, J. et al. Short-range ordered iridium single atoms integrated into cobalt oxide spinel structure for highly efficient electrocatalytic water oxidation. *J. Am. Chem. Soc.* **143**, 5201–5211 (2021).
61. Nong, H. et al. Key role of chemistry versus bias in electrocatalytic oxygen evolution. *Nature* **587**, 408–413 (2020).
62. Nong, H. et al. A unique oxygen ligand environment facilitates water oxidation in hole-doped IrNiO<sub>x</sub> core-shell electrocatalysts. *Nat. Catal.* **1**, 841–851 (2018).
63. Gao, J. et al. Breaking long-range order in iridium oxide by alkali ion for efficient water oxidation. *J. Am. Chem. Soc.* **141**, 3014–3023 (2019).
64. Casalongue, H. G. S. et al. A. In situ observation of surface species on iridium oxide nanoparticles during the oxygen evolution reaction. *Angew. Chem. Int. Ed.* **53**, 7169–7172 (2014).
65. Zhao, G., Li, P., Cheng, N., Dou, S. X. & Sun, W. An Ir–Ni(OH)<sub>2</sub> heterostructured electrocatalyst for the oxygen evolution reaction: breaking the scaling relation, stabilizing iridium (V), and beyond. *Adv. Mater.* **32**, 2000872 (2020).



66. Zheng, X. et al. Origin of enhanced water oxidation activity in an iridium single atom anchored on NiFe oxyhydroxide catalyst. *Proc. Natl. Acad. Sci. U.S.A.* **118**, e2101817118 (2021).
67. Zhao, Y. et al. Modulating Pt-O-Pt atomic clusters with isolated cobalt atoms for enhanced hydrogen evolution catalysis. *Nat. Commun.* **13**, 2430 (2022).
68. Seh, Z. W. et al. Combining theory and experiment in electrocatalysis: insights into materials design. *Science* **355**, eaad4998 (2017).
69. Kresse, G. & Furthmüller, J. Efficiency of ab-initio total energy calculations for metals and semiconductors using a plane-wave basis set. *Comp. Mater. Sci.* **6**, 15–50 (1996).
70. Kresse, G. & Furthmüller, J. Efficient iterative schemes for ab initio total-energy calculations using a plane-wave basis set. *Phys. Rev. B* **54**, 11169–11186 (1996).
71. Blöchl, P. E. Projector augmented-wave method. *Phys. Rev. B* **50**, 17953–17979 (1994).
72. Perdew, J. P., Burke, K. & Ernzerhof, M. Generalized gradient approximation made simple. *Phys. Rev. Lett.* **77**, 3865–3868 (1996).
73. Heyd, J., Scuseria, G. E. & Ernzerhof, M. Hybrid functionals based on a screened Coulomb potential. *J. Chem. Phys.* **118**, 8207 (2003).
74. Rossmeisl, J., Logadottir, A. & Nørskov, J. K. Electrolysis of water on (oxidized) metal surfaces. *Chem. Phys.* **319**, 178–184 (2005).
75. Bajdich, M., Garcia-Mota, M., Vojvodic, A., Nørskov, J. K. & Bell, A. T. Theoretical investigation of the activity of cobalt oxides for the electrochemical oxidation of water. *J. Am. Chem. Soc.* **135**, 13521–13530 (2013).

## Acknowledgements

The work leading to these results has received funding from the National Natural Science Foundation of China (22179098) and the Fundamental Research Funds for the Central Universities to J.M. Z.H. acknowledges support from the Max Planck-POSTECH-Hsinchu Center for Complex Phase Materials. The calculations were supported by the Welch Foundation (F-1841) and the Texas Advanced Computing Center to G.H. M.K. and P.S. acknowledge financial support by the Deutsche Forschungsgemeinschaft (DFG) through Project "Iridium" (STR 596/11-1) and by the Federal Ministry of Education and Research (BMBF) through the Verbundprojekt "HyThroughGen" (FKZ 03Hy108D) in the framework of the Leitprojekt "H2Giga". T.K. acknowledges support by the Deutsche Forschungsgemeinschaft (DFG) through the German-French Project "REALcharge" (STR 596/13-1).

## Author contributions

J.M. conceived and supervised the research. Y.Z. and J.M. designed the experiments. Y.Z., T.K., M.K., J.C., S.H., Z.H., P.S. and J.M. performed the experiments and data analysis. J.W., Y.Z. and G.H. performed the

theoretical computations and analyzed the theoretical results. Y.Z., T.K., J.C., S.H., Z.H., P.S. and J.M. participated in various aspects of the experiments and discussions. Y.Z., J.W., T.K., Z.H., P.S. and J.M. wrote the paper. All authors discussed the results and commented on the manuscript.

## Funding

Open Access funding enabled and organized by Projekt DEAL.

## Competing interests

The authors declare no competing interests.

## Additional information

**Supplementary information** The online version contains supplementary material available at <https://doi.org/10.1038/s41467-022-35426-8>.

**Correspondence** and requests for materials should be addressed to Zhiwei Hu, Peter Strasser or Jiwei Ma.

**Peer review information** *Nature Communications* thanks Subrata Kundu and the other, anonymous, reviewer(s) for their contribution to the peer review of this work.

**Reprints and permissions information** is available at <http://www.nature.com/reprints>

**Publisher's note** Springer Nature remains neutral with regard to jurisdictional claims in published maps and institutional affiliations.

**Open Access** This article is licensed under a Creative Commons Attribution 4.0 International License, which permits use, sharing, adaptation, distribution and reproduction in any medium or format, as long as you give appropriate credit to the original author(s) and the source, provide a link to the Creative Commons license, and indicate if changes were made. The images or other third party material in this article are included in the article's Creative Commons license, unless indicated otherwise in a credit line to the material. If material is not included in the article's Creative Commons license and your intended use is not permitted by statutory regulation or exceeds the permitted use, you will need to obtain permission directly from the copyright holder. To view a copy of this license, visit <http://creativecommons.org/licenses/by/4.0/>.

© The Author(s) 2022